Article

Photocatalytic Reduction of Cr(VI) and Pb(II) with Biogenically Synthesized Copper Oxide Nanoparticles Using an Extract of the *Myriophyllum spicatum* Plant

Opeyemi A. Oyewo *[ID] and Seshibe S. Makgato [ID]

Department of Chemical Engineering, College of Science, Engineering and Technology, University of South Africa (UNISA), c/o Christian de Wet Road and Pioneer Avenue, Florida Campus, Johannesburg 1710, South Africa; makgato2001@yahoo.com
* Correspondence: atiba.opeyemi@gmail.com

Abstract: The biogenic synthesis of copper oxide nanoparticles was explored using the *Myriophyllum spicatum* plant through a process involving co-precipitation and was utilized as an effective photocatalyst for the reduction of Cr(VI) and Pb(II) ions in an aqueous solution. The plant-mediated CuO nanoparticles were characterized using microscopic techniques (TEM and SEM), FT-IR, and XRD analyses. The amount of the reduced metal ions was determined by UV–visible and Atomic Absorption (AA) spectrophotometers. The analyses of the functional group present in the leaf extract revealed the type of bioactive molecules that were involved in the formation of copper oxide nanoparticles. The nanoparticles were used in the photo-enhanced reduction of hexavalent Cr and divalent Pb ions, and the impact of solution pH, initial metal concentrations, and photocatalyst dosage was investigated to establish the optimal performance of the CuO nanoparticles. Results revealed a direct association between the reduction of metal ions and catalyst dosage in both cases. A maximum percentage reduction of 89.2% and 79.1% was achieved for Cr(VI) and Pb(II), respectively, using 3 g of the CuO nanoparticles. This confirms that the CuO nanoparticles exhibited higher efficiency for Cr(VI) reduction as compared to Pb(II) reduction and indicates that CuO nanoparticles are a promising photocatalyst that is capable of reducing these metal ions into less toxic products.

Keywords: biogenic synthesis; copper oxide; photocatalyst; *Myriophyllum spicatum* plant

1. Introduction

Chromium and lead are well-known metals that have found useful applications in industry. However, in their ionic form, specifically hexavalent chromium and divalent lead, they pose some health hazards to humans, plants, and other living organisms. Thus, they are regarded worldwide as prioritized toxic pollutants. The presence of these toxic metal ions in domestic water may be attributed to natural sources or activities that include the disposal of effluents into the environment by industries such as leather, ceramic, steel, and alloy-producing industries [1]. High concentrations of chromium and lead in humans through water consumption are dangerous since these ions are mutagenic and carcinogenic [2].

Hexavalent chromium is highly toxic to the human body, and its good solubility in solution improves the active transport of chromate across biotic membranes [3]. Therefore, it has a diverse range of negative health effects, such as gingivitis, chronic bronchitis, pneumonitis, lung cancer, respiratory tract disease, and liver and kidney diseases [4]. Similarly, exposure to lead also causes health issues such as brain and central nervous system damage, anxiety, delusions, the inhibition of hemoglobin formation, increased aggression, mania, and suicidal tendencies. Furthermore, the inhalation of lead could result in its accumulation in the system and may cause kidney damage, colic pains, miscarriage, liver disorder, loss of appetite, and cancer [5].

Due to changes in physicochemical conditions, the reaction of various forms of Cr and Pb found in water may vary due to their different sources compared to other heavy metals. The concentration of chromium and lead in surface waters is usually low and at the µg/L level, often between 0.3 and 6 µg/L [6]. However, the maximum allowable limit for Cr(VI) and Pb (II) in drinking and industrial water (as recommended by the WHO) is from 0.05 to 5 mg/L and 0.01 to 0.15 mg/L, respectively [7–9]. The speciation of these metal ions has been a longstanding analytical challenge, and their selective determination is necessary due to their toxicity [10]. Due to serious environmental regulations imposed on the use of these species, mineral processing or metal-finishing industries continue to inspire studies on the appropriate disposal route of Pb- and Cr-laden effluents.

Chromium and lead ion removal has been achieved by ion exchange [11,12], adsorption [13,14], precipitation [15,16], and photocatalytic processes [17]. The hydroxides of most heavy metals are usually insoluble; therefore, lime is commonly used to precipitate them from water. The colloidal state of the precipitated materials is one of the challenges faced by this process in reaching the desired effluent limits, and this has limited the performance of this method [18]. Several studies have reported Pb(II) and Cr(VI) removal from water using adsorption techniques and efficient adsorbents [19]. Despite the effectiveness of this process, the production of secondary waste remains a major drawback associated with the use of the adsorption process [20,21]. These drawbacks can be alleviated by employing a photocatalytic approach that completely reduces Cr(VI) and Pb(II) into less harmful and useful materials [22]. Thus, this offers an additional advantage and has high economic feasibility for industries, provided that an appropriate and eco-friendly photocatalyst is utilized.

Several semiconductor nanoparticles, such as ZnO [23], TiO_2 [24], and CuO [25], have been used for the reduction of these metal ions into less harmful materials. The synthesis route and the properties of the nanoparticles influence their performance. For instance, heterojunction systems or plant extract-based nanocomposites have been reported to exhibit higher efficiency compared to single or unmodified semiconductors [26]. In plant-mediated synthesis, the choice of the synthesized nanoparticles, the route/method used in the synthesis, and the type of the phytocomponents determine the performance of the catalyst in the reduction process of the target metals [27]. For example, CuO has been synthesized via different synthesis routes, such as the alcohol–thermal approach [28,29], microwave irradiation [30], the precipitation method [31], and the biogenic approach [32]. It has been reported that the biogenic approach using a suitable plant extract [32,33] is more efficient, economical, and environmentally friendly. CuO synthesized using plant extract has been used for the degradation of dyes [34] and organic compounds [35]. In addition, the efficiency of CuO nanoparticles in Cr(VI) and Pb(II) removal from water has been reported [36,37]. Therefore, the synthesis of CuO using a *Myriophyllum spicatum* extract was explored for Cr(VI) reduction.

Myriophyllum spicatum is a submerged aquatic plant that is known to grow in still or slow-moving water. It originated from North Africa, Asia, and Europe, but it is also distributed across the globe, extending from northern Canada to South Africa. It is considered to be a highly invasive species and was first found in southern Africa in 1829 near the Vaal River [38]. *Myriophyllum spicatum* leaves are abundantly available, cost-effective, and possess functional groups that could enhance photocatalytic activity. Therefore, they were selected for this study [39].

In this study, an aqueous extract of *Myriophyllum spicatum* was used to mediate the synthesis of CuO nanoparticles, which was used as a photocatalyst for the reduction of Cr(VI) and Pb(II) from water. Biogenic synthesized CuO nanoparticles were characterized to establish the physiochemical properties using structural, spectroscopic, and morphological techniques. The photocatalytic efficiency for the reduction of Pb(II) and Cr(VI) was evaluated, and key operating parameters, such as initial metal ions (Pb(II) and Cr(VI)) concentration, initial pH, and catalyst dosage and were studied to establish the performance of green-based CuO nanoparticles.

2. Experimental Section

2.1. Materials

Fresh *Myriophyllum spicatum* leaves were collected from the Vaal River, South Africa, and were properly identified. A total of 0.1 M HCl and NaOH were used to alter the initial pH. Copper acetate, potassium dichromate, and lead nitrate salts were purchased from Sigma-Aldrich, Pretoria, South Africa. The deionized water used for solution preparation was processed by the Model Select Analyst HP40 (UK). All chemicals used were of analytical grade.

2.2. Myriophyllum spicatum Leaf Extract's Preparation

Myriophyllum spicatum leaves were collected, double-washed with purified water to remove the adhering dirt, and then shade-dried for 7 days [40,41]. About 8 g of blended leaves were added to 80 mL of deionized water and then heated at 70 °C for 5 h. The mixture was then filtered and cooled to 25 °C before being stored in a refrigerator.

2.3. Biogenic Synthesis of CuO Nanoparticles

Biogenic CuO-NPs were synthesized following the reported procedure by Singh et al. [42]. Copper acetate monohydrate was used as a base precursor, and about 4 g was dissolved in a known amount of purified water and stirred continuously for 10 min. A total of 20 mL of *Myriophyllum spicatum* extract (pH value 7.2) was added to the copper acetate monohydrate drop-wise, and the solution color changed to darkish brown upon the addition of the leaf extract. While stirring, the solution was heated at 80 °C for 4 h. The solution was centrifuged, dried at 90 °C overnight, and then calcinated at 400 °C for 4 h.

2.4. Characterization of the Prepared CuO Nanoparticles

The functional group in the plant was analyzed using FT-IR spectroscopy by a Perkin Elmer Spectrum 100 spectrometer, and the measurement was recorded between 500 and 4000 cm^{-1} at a resolution of 4 cm^{-1}. Absorption measurements were carried out using a Varian UV–Vis spectrophotometer. A Bruker D8 Advanced XRD machine was used for the diffraction pattern of the sample, and the obtained patterns were compared to the standard JCPDS database [43]. Morphological properties were studied using a JEOL 6400F Field Emission SEM at 5 kV and Hitachi HF–2000 TEM at 200 kV.

2.5. Photocatalytic Reduction of Cr(VI) and Pb(II) in Water

The reduction of the Cr(VI) and Pb(II) ions in simulated water was investigated separately using plant-based CuO nanoparticles under visible light irradiation. A circulating water source in the reactor vessel with a 250–W Xe discharge lamp was used. About 50 mg/L concentration of both metal ions and 1–3 g of the CuO nanoparticles were used. The nanoparticles were introduced into the aqueous pollutant's solution and stirred magnetically in the dark for one hour until the adsorption equilibrium was reached. The mixture was then irradiated with the visible lamp for 90 min of continuous stirring. The aliquots were taken from the solution after 5 min and subsequently at 10 min intervals over a 90 min period. The degradation efficiency of the chromium and lead ions was studied using a UV–Vis spectrophotometer and an Atomic Absorption Spectrophotometer (AAS). The photocatalytic reduction of Pb(NO) was observed by AAS at wavelength 217.0 nm.

The percentage photocatalytic reduction of both Cr(VI) and Pb(II) ions was calculated using the following equation:

$$\text{Reduction yield } \% = \frac{C_0 - C_e}{C_0} \times 100 \tag{1}$$

where C_0 is the initial concentration, and C_e is the concentration of metals after a specific time.

3. Results and Discussion

3.1. X-ray Diffraction (XRD) Studies

The formation of copper oxide NPs using *Myriophyllum spicatum* plant extract was confirmed by XRD analysis, and the diffraction pattern is presented in Figure 1. The patterns displayed peaks located at 2θ = 36.18° and 39.17°, which are assigned to the planes of (−111) and (111), respectively [44]. This corresponds to the standard card number of ICSD 98-006-9757 [45], and there are no characteristic impurity peaks of CuO, Cu_2O, or $Cu(OH)_2$ nanoparticles displayed in the XRD pattern, indicating that a pure monoclinic crystalline structure of CuO nanoparticles was formed [46]. The crystal structure of CuO nanoparticles in Figure 1 shows how the Cu and O atoms are arranged in the crystal lattice of CuO, in which the Cu atom is coordinated by four coplanar O atoms like a rectangular parallelogram. Copper atoms have the large spheres, and O atoms have the smaller spheres. The shaded part in the crystals is two CuO_2 chains [47]. The CuO forms two different ribbons of parallelograms in the (110) and ($\bar{1}$10) directions [48]. The average crystalline size of the CuO-NPs calculated by the Scherer formula was to be around 32.54 nm.
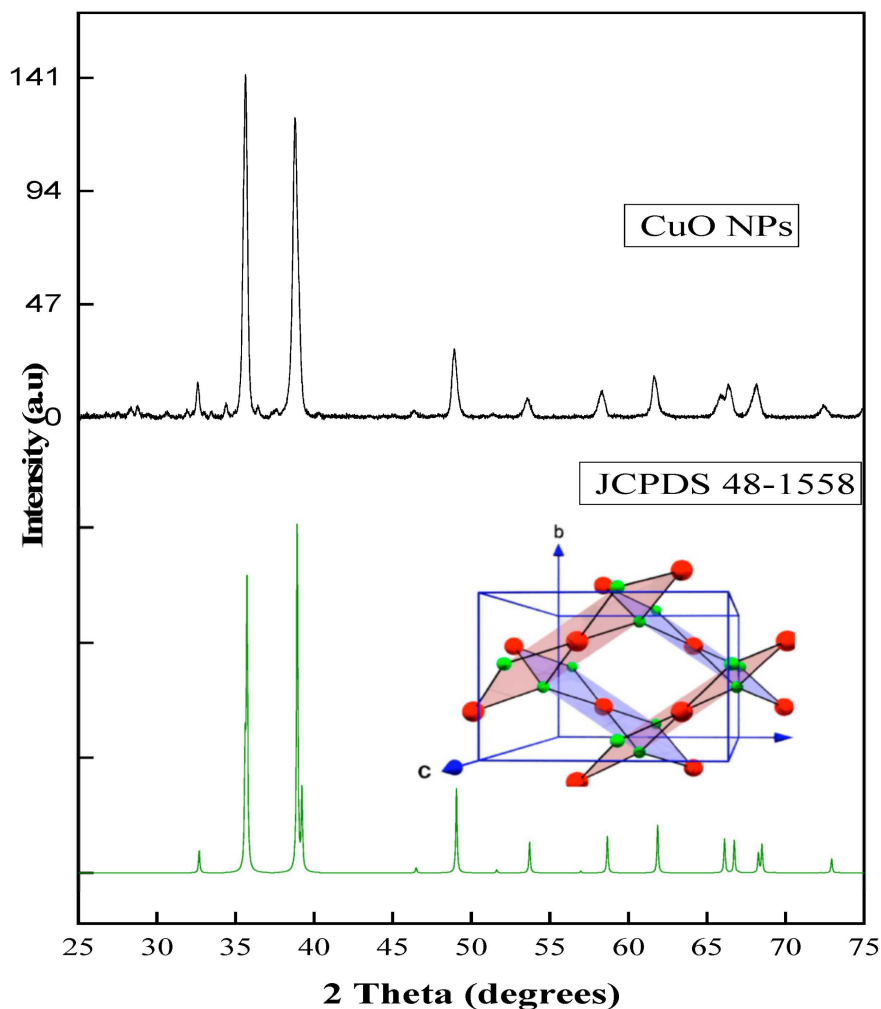
Figure 1. XRD of CuO nanoparticles synthesized using aqueous extract of *Myriophyllum spicatum* plant. Inset is the crystal structure showing copper atoms (red spheres) and oxygen atoms (green spheres) [47].

3.2. Fourier Transform Infrared (FT-IR) Spectroscopy

FT-IR analysis was used to identify the functional groups present in the plant, and the spectrum is shown in Figure 2. These bioactive molecules present in the leaf extract *Myriophyllum spicatum* play a role in mediating the nanoparticle synthesis. In the spectrum,

the broadband in the 3263–3550 cm^{-1} vibrational frequency is the O-H stretching vibration, while the absorption peak at 2919 cm^{-1} is attributed to the C-H vibration of saturated carbon. This peak appears at slightly below 3000 cm^{-1} and often appears at a lower frequency than the C-H of unsaturated carbon, which appears at slightly beyond 3000 cm^{-1}. The peaks at 1721 cm^{-1} and 1247 cm^{-1} are ascribed to C=C and C-OH stretching, respectively. The band, which appears at 564 cm^{-1}, is attributed to the vibration due to the Cu-O bond, and this confirms the synthesis of CuO nanoparticles [49]. These functional groups are indicative of the presence of phytochemicals such as tannins, flavonoids, proteins, carboxylic acids, and alkaloids in the formation of CuO nanoparticles [49,50]. The observed peaks are similar to the vibrational bands reported for CuO nanostructures in other studies [51,52].
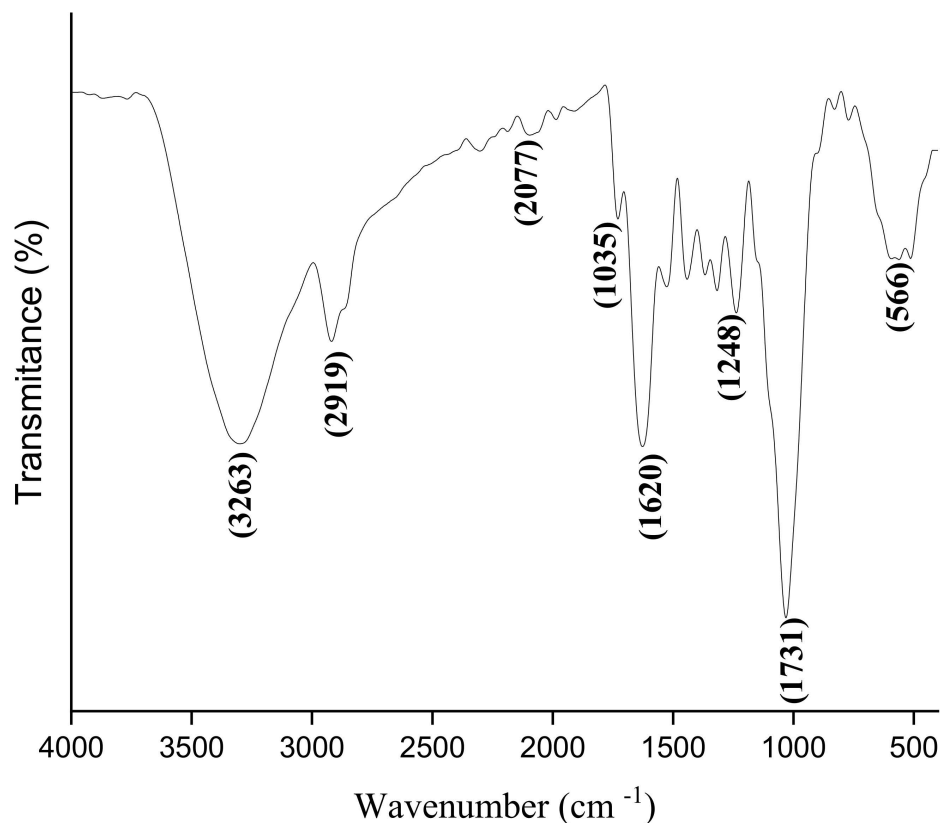
Figure 2. FT-IR spectrum prepared from the extract of the *Myriophyllum spicatum* plant.

Figure 3 presents the UV–Vis spectrum of CuO. Absorption spectroscopy is the most important method of analysis for CuO NP surface plasmon resonance (SPR) detection. This property is a phenomenon that occurs due to the collective oscillation of electrons in the conduction band that is in resonance with the oscillating electric field of the incident light, leading to the production of energetic plasmonic electrons via non-radiative excitation [53]. Therefore, the absorbance peak at 384 nm is attributed to copper oxide, which is in agreement with some related studies on the plant-mediated biosynthesis of CuO-NPs [54–56].
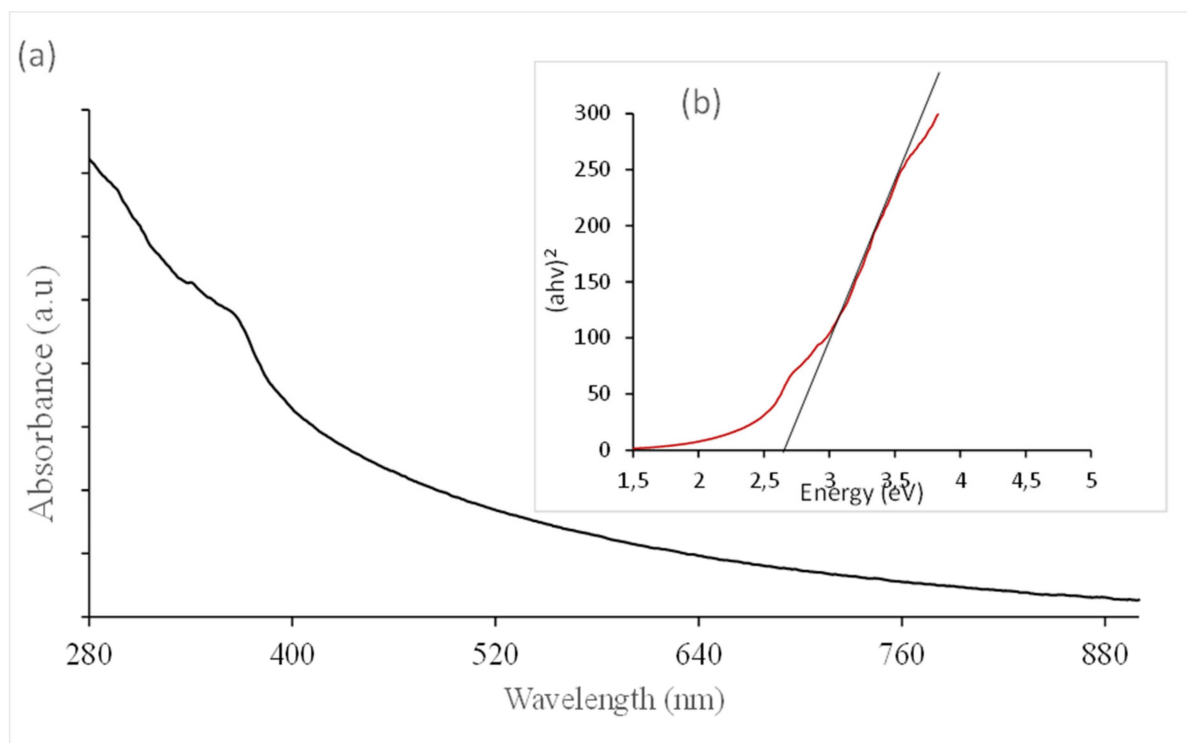
Figure 3. (**a**) UV–Vis spectrum, and (**b**) Tauc plot of CuO (inset) prepared from the extract of the *Myriophyllum spicatum* plant.

The band-gap energy of the CuO nanoparticles was estimated using the Tauc plot and Equation (2) for a direct transition in semiconductors, which is given by:

$$(\alpha h\gamma) = c(hv - Eg) \qquad (2)$$

where $h\gamma$ and α are the incident energy of the photon and the absorption coefficient, respectively; c is a constant; and Eg represents the band-gap energy. A plot of $(\alpha h\gamma)^2$ versus the photon energy ($E = h\gamma$) gives the value of the band-gap energy as the intercept on the x-axis, as shown in the inset of Figure 3. The band-gap energy was obtained as 2.65 ev, which is a blue shift in terms of the bulk CuO (1.85 eV) [57]. This variation could be attributed to the consequence of the quantum confinement effect emanating from the reduction in the nanoparticle's size [58,59] and similar to the values reported for previous studies [60,61].

3.3. Morphological Studies

As well as providing information on the surface morphology, SEM analysis also displays the structure and degree of agglomeration of nanoparticles [27]. The SEM micrographs of copper oxide nanoparticles at different magnifications are evenly distributed and homogeneous (Figure 4a,b). Both magnifications show the spherical morphology of the as-synthesized CuO nanoparticles. This observation is also confirmed by TEM analysis (Figure 4c), which presents spherical particles with obvious agglomeration that is often associated with high-temperature products [62,63]. It was evident that CuO-NPs were poly-dispersed and spherical. The particles were in the size range 21–42 nm, and the average particle size was 29 nm. The mapping image shows evenly distributed particles, which confirms that the copper and oxygen were well distributed across the matrices of the metal oxide nanoparticles (Figure 4d–f). Figure 4g presents the EDS analysis of synthesized CuO nanoparticles, which displays copper (Cu) and oxygen (O) as the main components in the spectrum. The weight percentage of copper and oxygen was calculated to be 73.15 and

22.17%, respectively. A similar observation was reported in previous work on Cu NPs and CuO-NPs [31,64].
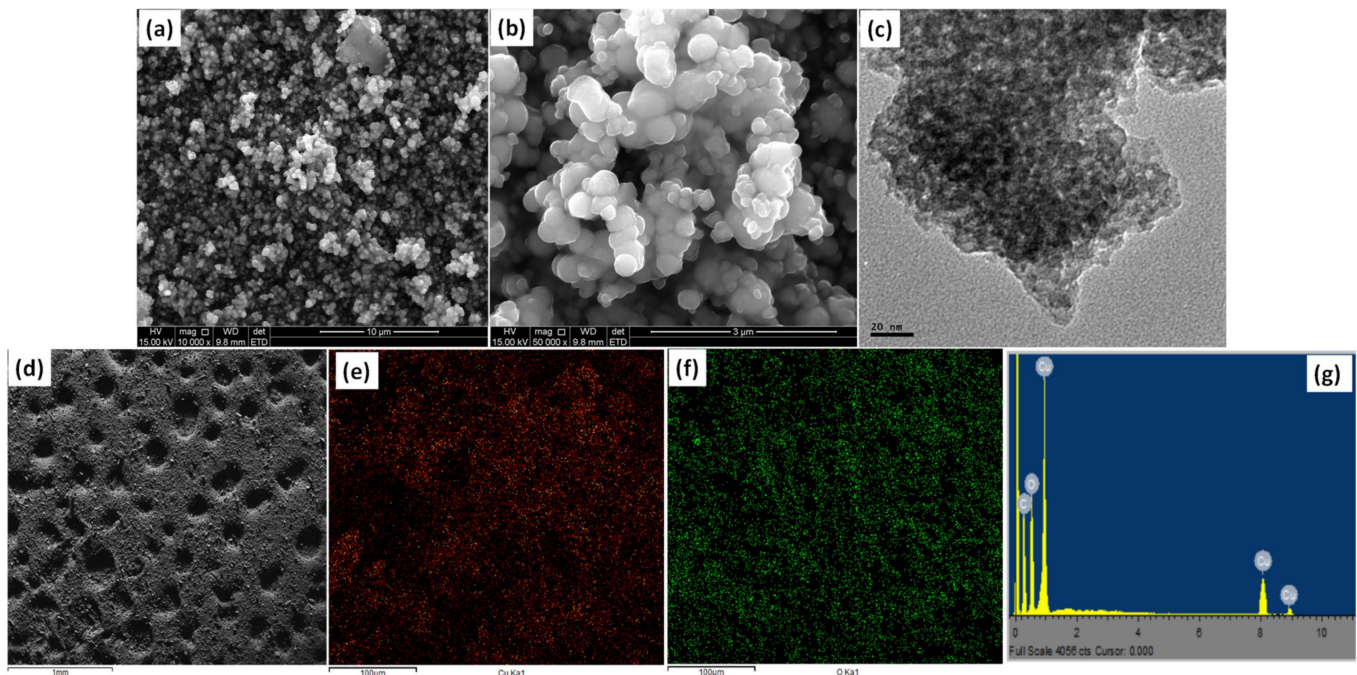
Figure 4. SEM at (**a**) low and (**b**) high magnification; (**c**) TEM micrograph; (**d**) elemental mapping; (**e**) Cu and (**f**) O; (**g**) EDX spectra of CuO nanoparticles prepared from the aqueous leaf extract of the *Myriophyllum spicatum* plant.

3.4. Photocatalyst Reduction of Cr(VI) to Cr(III) and Pb(II) to Pb(0)

The existence of hexavalent chromium is in three different ionic forms, which include $HCrO_4^-$, CrO_4, and $Cr_2O_7^{2-}$ [65]. The hexavalent chromium species are predominated in different solution pHs. Chromium ions exist in both neutral and basic media, while the hydro chromium can be found in lower pHs.

The amount of Cr(VI) or Pb(II) remaining at any given time was calculated using the relationship shown in Equations (3) and (4):

$$\left[Cr_{(Tot)}\right] - [Cr(VI)] = [Cr(III)], \tag{3}$$

$$\frac{\left[Cr_{(Tot)}\right] - [Cr(VI)]}{\left[Cr_{(Tot)}\right]} \tag{4}$$

Therefore, three stages are involved in the reduction of Cr(VI) to Cr(III). First, Cr(VI) reduces to Cr(V) by reducing the molecular oxygen to hydrogen peroxide. After that, Cr(V) produces hydroxyl radicals and then produces intermediates, which are Cr(IV), free radicals, and Cr(III) as the final product [66,67].

Idris et al. [68] reported the reduction of Pb(II) to Pb(0), which usually occurs at acidic suspension pH, and the color changes could be observed on the photocatalyst surface at the end of the experiment, which confirms the photocatalytic response. Metallic lead was observed as a black deposit on the photocatalyst (CuO) after the run, which can be identified as PbO^2. Murruni et al. [69], who reported the photocatalytic removal of Pb(II) using Pt–TiO$_2$ powders, suggested the validity of a similar pathway for Pb(II) reduction to metallic lead as follows:

$$Pb^{2+} + e^- \rightarrow Pb^+ \tag{5}$$

$$Pb^+ + e^- \rightarrow Pb(0) \tag{6}$$

3.5. The Effects of Solution pH on the Cr(VI) and Pb(II) Reduction

The solution pH was investigated to establish the impact of surface charge, which depends on the pH of the solution being positive in an acidic medium and negative in an alkaline medium. Figure 5a,b display the impact of solution pH in the photocatalytic reduction of Cr(VI) and Pb(II), respectively. pH 4–8 was investigated in the reduction of both toxic metals onto CuO nanoparticles. Surprisingly, a similar trend was observed in both metal ions; however, CuO-NPs have a higher affinity for Cr(VI) compared to Pb(II) at the optimum pH of 4.2 [70]. For example, at a low pH of the solution, a higher reduction of both Pb(II) and Cr(VI) occurred. As the pH increased, the reduction of both metal ions decreased. This might be due to the decrease in the amount of H^+ ions in the solution. The electrostatic interaction between the positively charged metal ions and the negatively charged site of nanoparticles might be the main mechanism that governs the reduction of these ions in water. Therefore, the fate of the photocatalytic reduction of these metal ions depends on the surface charge of the semiconductor–electrolyte interface.
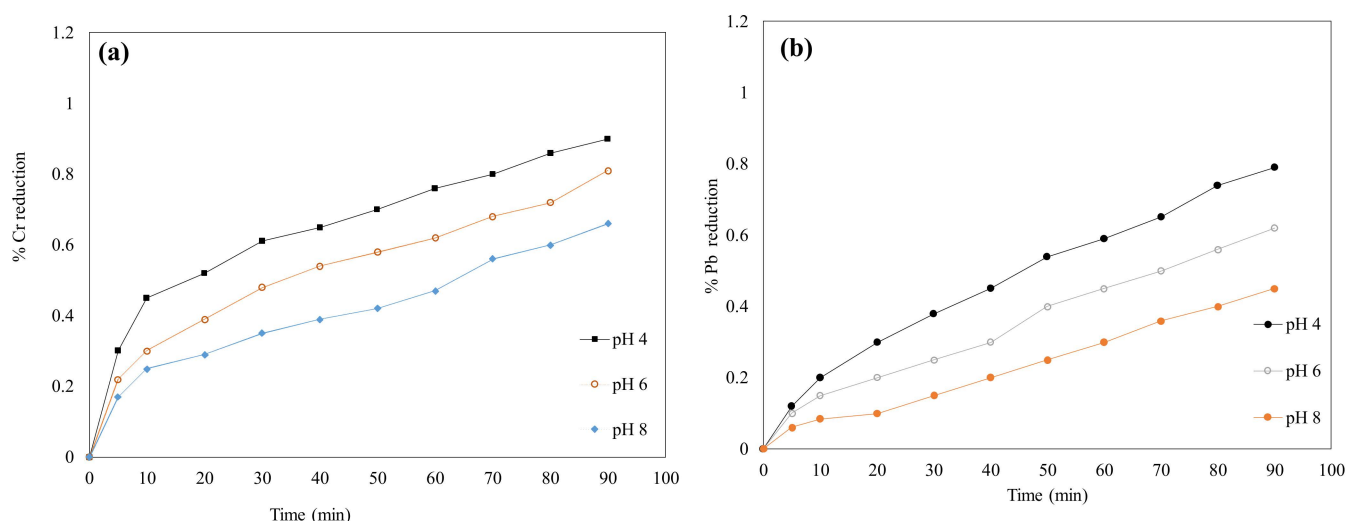
Figure 5. Effect of solution pH on the reduction of (**a**) Cr(VI), and (**b**) Pb(II) using plant-based CuO (conc. of photocatalyst = 3 g/L, conc. = 50 mg/L).

3.6. Effect of Catalyst Dosage on the Metal Reduction Process

The quantity of nanoparticles used to treat a liter of water has an impact on the rate of reduction of metal ions in water. As is evident in the plot presented in Figure 6a,b, the photocatalytic reduction rate of Cr(VI) and Pb(II) increases with an increase in catalyst dosage. However, the rate of both metal reductions became constant with the use of 3 g/L, and little or no further increase in the reaction rate was observed beyond the usage of 3 g. This is an indication that more particles are available for excitation with an increase in catalyst dosage. Therefore, there might be a greater possibility of electron–hole pair generation upon exposure to light [71]. A maximum percentage reduction of 90.2% and 79.1% was achieved for Cr(VI) and Pb(II), respectively, with the use of 3 g of CuO nanoparticles.
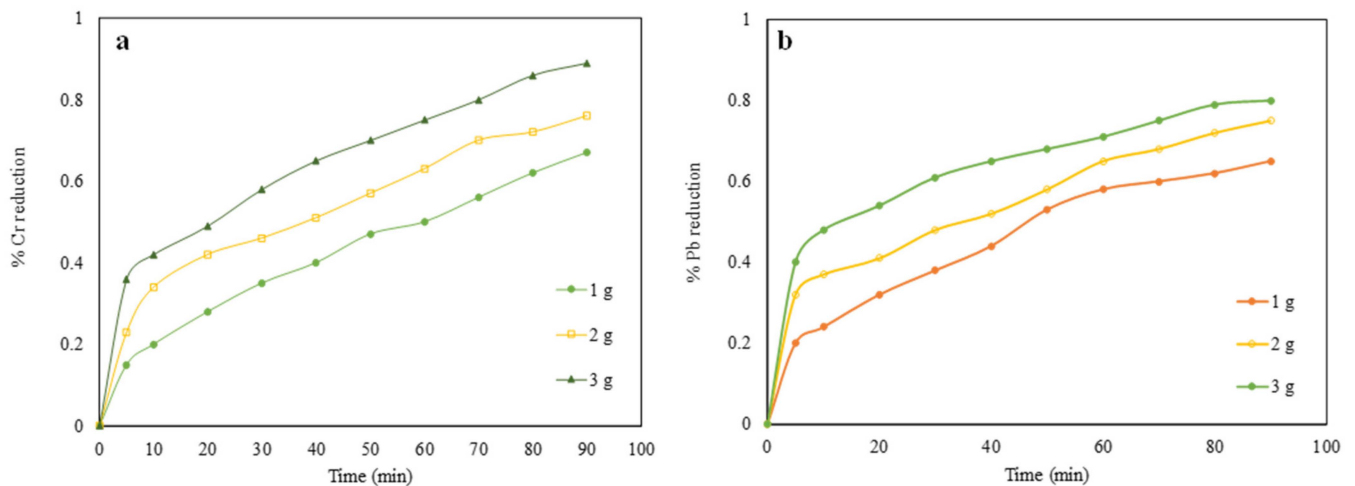
Figure 6. The effect of catalyst loading on the reduction of (**a**) Cr(VI) and (**b**) Pb(II) using CuO (conc = 50 mg/L, pH = 4, irradiation time = 90 min).

3.7. Effect of the Concentration of Metals on Their Reduction Process

The concentration of both ions varied between 25 and 100 mg/L, and the influence of change in concentration on the reduction of ions was observed, as shown in Figure 7a,b. An indirect relationship between concentration increases and the rate of reduction of the metal ions was observed. This might be because the movement of both ions towards the semiconductor surface was hindered due to the high concentration of metal ions. Therefore, Cr(VI) and Pb(II) ions were not permitted to reach the desired active site within the time domain and, therefore, decreased the rate of ion reduction in water [72].
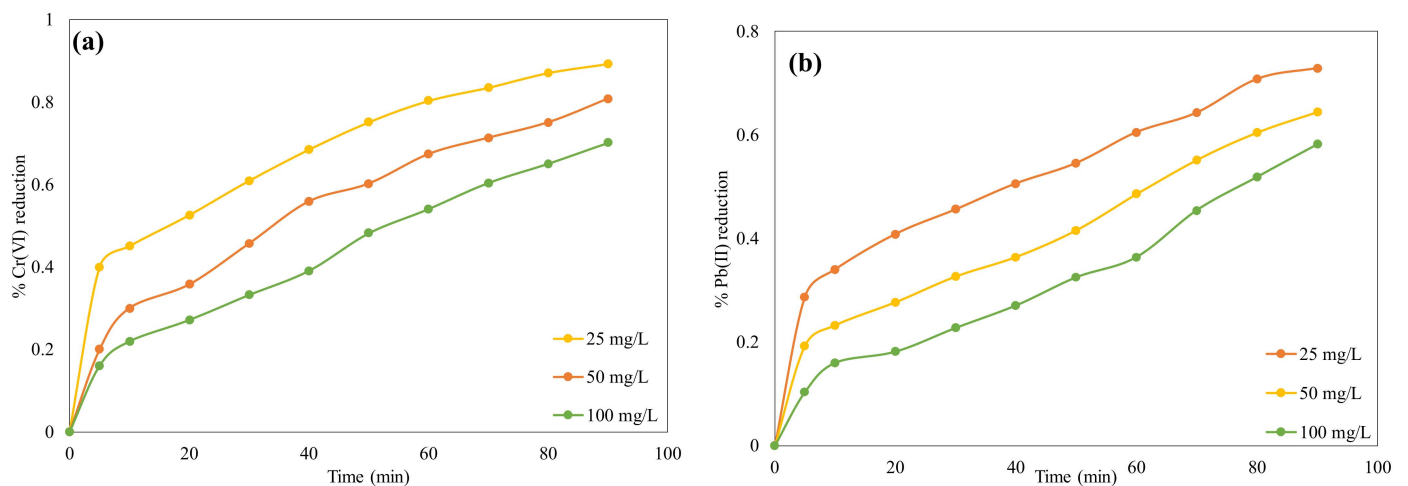
Figure 7. The effect of (**a**) Cr(VI) and (**b**) Pb(II) concentration on the photoreduction process using CuO nanoparticles (conc of photocatalyst = 3 g/L, pH = 4, irradiation time = 90 min).

The gradual reduction of both metal ions can be observed with a decrease in initial metal ion concentration (Figure 8). The ultrafast charge carrier separation and photo absorption might be responsible for the highest reduction activity obtained with the use of biogenic CuO. According to the results obtained for Cr(VI) and Pb(II), the optimum catalyst loading amount of 3 g/L exhibited a higher photocatalytic reduction in Cr(VI) as compared to Pb(II) reduction in the solution [73]. As such, the intensity of Cr (VI) ion absorption peaks decreases with increasing irradiation time, and about 89.2% reduction of Cr (VI) to Cr(III) was achieved within 90 min. A color change from yellow to colorless confirmed the reduction of toxic chromium in the solution [74]. A similar reduction pattern or mechanism was observed in the reduction of Pb(II) to Pb(0); however, biogenic

CuO seems to have a higher affinity for Cr(VI) compared to Pb(II). Therefore, about a 79.1% reduction of toxic lead was achieved. The experiment performed in the dark to achieve the adsorption–desorption equilibrium for both metal ions could be considered insignificant under the same conditions because only 3% and 2% reduction of Cr(VI) and Pb(II), respectively, were recorded. This therefore indicated the importance of light in the reduction process.
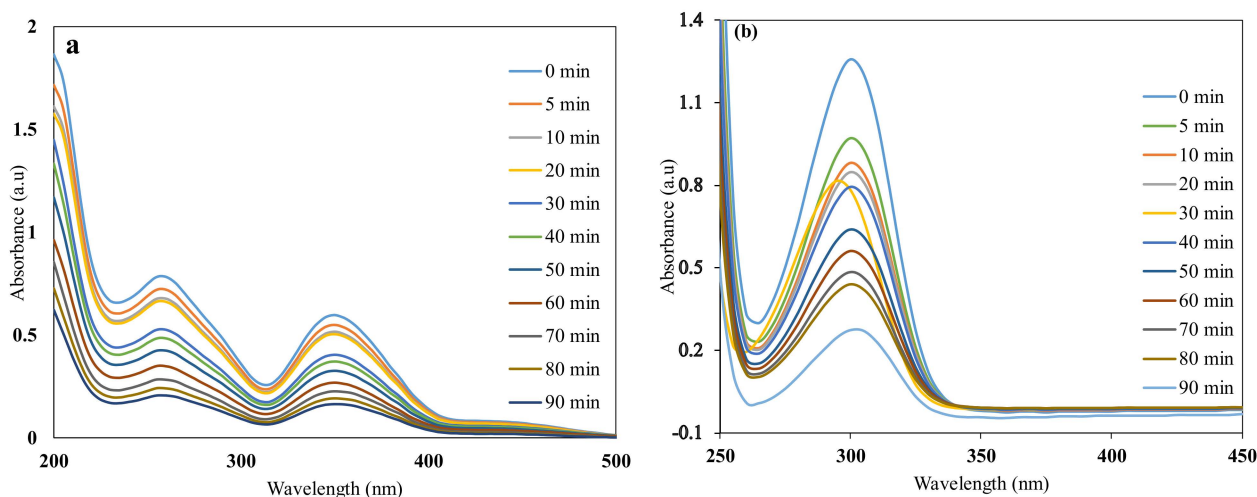
Figure 8. UV–Vis absorption spectra of photocatalytic reduction of (**a**) Cr(VI) and (**b**) Pb(II) ions using biogenic CuO nanoparticles.

3.8. Mechanism of the Biogenic CuO Photocatalytic Process in the Reduction of Cr(VI) and Pb(II)

A schematic diagram of the photocatalytic activity of the biogenic CuO nanoparticles is presented in Figure 9. When holes are generated in the valence band, a source of light induces electrons to excite from the valence to the conduction band [75]. The H_2O molecules in the reaction are oxidized by holes to more reactive OH radicals. Therefore, the oxygen molecule is reduced to O^{-2} radicals due to the presence of excited electrons in the conduction band, and H_2O_2 is reduced to OH radicals, too. The reduction of Cr(VI) and Pb(II) to Cr(II) and Pb(0), H_2O, and other mineralization products can be attributed to the oxide and hydroxyl radicals formed by CuO nanoparticles [76]. The study also observed from Table 1 that the current approach gave a very good metal ion reduction compared to other CuO-based photocatalysts.

3.9. Reusability of the Copper Oxide Nanoparticles on Cr(VI)

The stability of the biogenic copper oxide nanoparticles on Cr(VI) reduction was investigated to establish the robustness of the nanoparticles after a few runs. About 3 g/L CuO was used in four cycles using a solution of 25 mg/L of Cr(VI), and the result is presented in Figure 10. After each cycle, the CuO catalyst was filtered, dried, and used for the next experiment. The CuO nanoparticles were found to be moderately stable up to their fourth cycle [77]. Although the Cr(VI) reduction decreases as the reusability cycle increases from cycles 1–4, stability was maintained because the difference between the performance of the catalyst is insignificant [78]. A decrease from 89.2 to 70% Cr(VI) reduction was noticed as the reusability cycle increased from the first to the fourth cycle. This observation could be attributed to the accumulation of byproducts on the active surface sites of the catalyst and the loss of some amount of catalyst during the filtration process. Ravele et al. [79] reported that the economic value of any photocatalyst in water treatment can be determined by the cycling stability test because less photocatalyst would be needed to reduce Cr(VI) from water, therefore saving some cost. Similar observations have been reported in other studies [80,81].
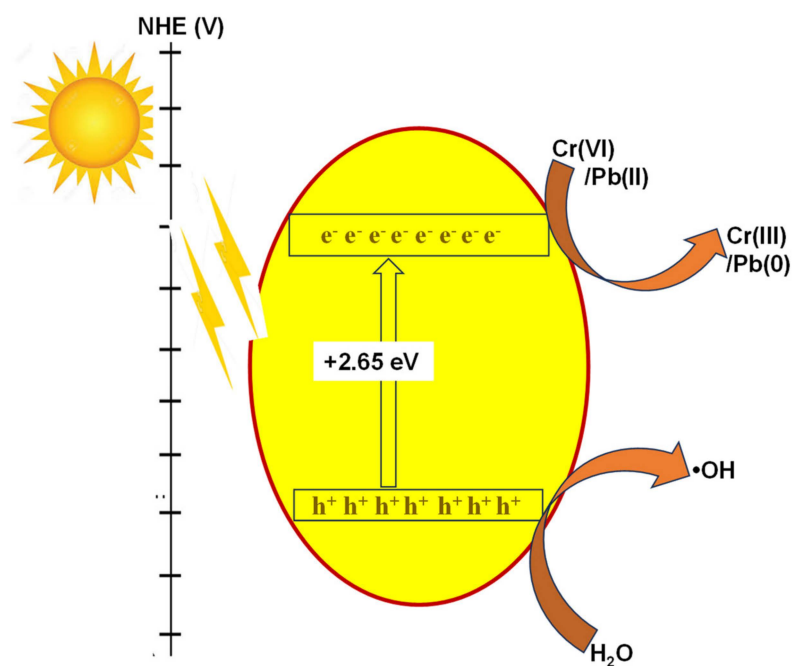
Figure 9. Schematic diagram of biogenic CuO photocatalysts in the reduction of Cr(VI) and Pb(II).
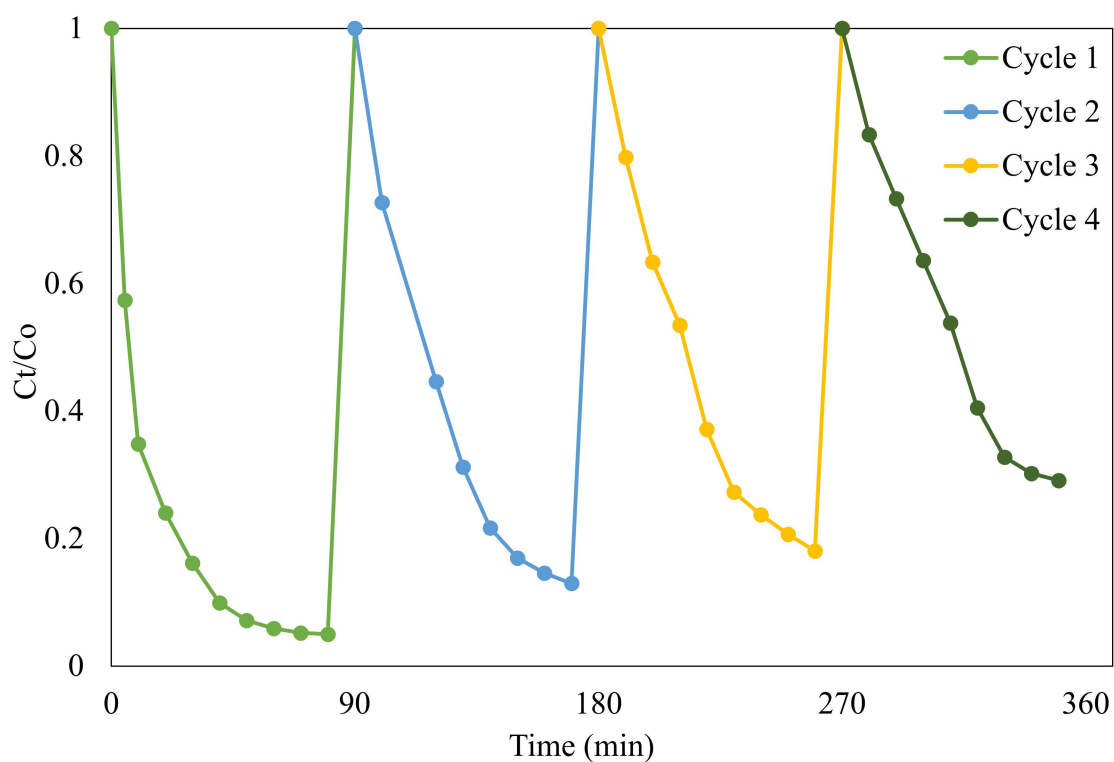
Figure 10. Reusability cycles of Cr(VI) reduction using 3 g/L of biogenic synthesized copper oxide nanoparticles and a solution of 25 mg/L Cr(VI).

The high reduction percentage obtained with the use of the biogenic CuO nanoparticles compares favorably with other CuO-based nanoparticles reported in other studies (Table 1).

Table 1. Comparison of photocatalytic reduction values obtained from CuO nanoparticles with the percentage Cr(VI) reduction of different CuO-based photocatalysts, as reported in the literature.

Photocatalysts	*Pollutant Treated*	*% Reduction*	*References*
Biogenic CuO nanoparticles	Cr(VI)	89.2	This study
CuO-Kaolin	Cr(VI) in electroplating wastewater	79.6%	[80]
Cupriavidus basilensis CuO	Cr(VI)	44.7%	[81]
CuO-ceramic ultrafiltration membrane	Cr(VI)	88.08%	[82]
Doped CuO	Cr(VI)	72%	[83]
Undoped CuO	Cr(VI)	56%	[83]

4. Conclusions

The synthesis and application of CuO nanoparticles mediated by the extract of *Myriophyllum spicatum* in the reduction of Cr(VI) and Pb(II) ions under visible light was investigated. The as-synthesized nanoparticles were characterized by XRD, SEM, TEM EDX, and UV–Visible spectroscopy. Fourier transform infrared analysis confirmed the existence of phytochemicals induced by the plant extract during the synthesis of the copper oxide nanoparticles. X-ray diffraction analysis of the particles revealed the formation of CuO with a monoclinic phase. Photocatalytic analysis indicated that plant-based CuO nanoparticles exhibited superior reduction efficiency of Cr(VI) (89.2%) compared to Pb(II) 79.1%. As pH increased from 4 to 8, reduction efficiency decreased. An increase in catalyst dosage was found to be directly proportional to the reduction of Cr(VI) and Pb(II), while an increase in the concentration of Cr(VI) impeded the removal process.

References

1. Barnhart, J. Occurrences, Uses, and Properties of Chromium. *Regul. Toxicol. Pharmacol.* **1997**, *26*, S3–S7. [CrossRef] [PubMed]
2. Sharma, S.K.; Petrusevski, B.; Amy, G. Chromium removal from water: A review. *J. Water Supply Res. Technol.* **2008**, *57*, 541–553. [CrossRef]
3. Ray, R.R. Adverse hematological effects of hexavalent chromium: An overview. *Interdiscip. Toxicol.* **2016**, *9*, 55. [CrossRef] [PubMed]
4. Cohen, M.D.; Costa, M. Chromium compounds. *Environ. Occup. Med.* **1998**, *2*, 799–805.
5. Sharma, J.C.; Vijay, A.; Bhardwaj, S. Photocatalytic activity of a novel compound SrWO4: Removal of toxic metal lead (II) from water. *World Appl. Sci. J.* **2013**, *23*, 208–212.
6. Vernay, P.; Gauthier-Moussard, C.; Hitmi, A. Interaction of bioaccumulation of heavy metal chromium with water relation, mineral nutrition and photosynthesis in developed leaves of *Lolium perenne* L. *Chemosphere* **2007**, *68*, 1563–1575. [CrossRef]
7. Zhao, R.; Li, X.; Sun, B.; Li, Y.; Li, Y.; Yang, R.; Wang, C. Branched polyethylenimine grafted electrospun polyacrylonitrile fiber membrane: A novel and effective adsorbent for Cr (VI) remediation in wastewater. *J. Mater. Chem. A* **2017**, *5*, 1133–1144. [CrossRef]
8. Sarin, V.; Pant, K. Removal of chromium from industrial waste by using eucalyptus bark. *Bioresour. Technol.* **2006**, *97*, 15–20. [CrossRef]
9. WHO. *Guidelines for Drinking-Water Quality*; World Health Organization: Geneva, Switzerland, 2004; Volume 1.

10. Rakhunde, R.; Deshpande, L.; Juneja, H.D. Chemical speciation of chromium in water: A review. *Crit. Rev. Environ. Sci. Technol.* **2012**, *42*, 776–810. [CrossRef]
11. Rengaraj, S.; Yeon, K.-H.; Moon, S.-H. Removal of chromium from water and wastewater by ion exchange resins. *J. Hazard. Mater.* **2001**, *87*, 273–287. [CrossRef]
12. Rengaraj, S.; Joo, C.K.; Kim, Y.; Yi, J. Kinetics of removal of chromium from water and electronic process wastewater by ion exchange resins: 1200H, 1500H and IRN97H. *J. Hazard. Mater.* **2003**, *102*, 257–275. [CrossRef] [PubMed]
13. Huang, C.P.; Wu, M.H. Chromium removal by carbon adsorption. *Water Pollut. Control Fed.* **1975**, *47*, 2437–2446.
14. Khalifa, E.B.; Rzig, B.; Chakroun, R.; Nouagui, H.; Hamrouni, B. Application of response surface methodology for chromium removal by adsorption on low-cost biosorbent. *Chemom. Intell. Lab. Syst.* **2019**, *189*, 18–26. [CrossRef]
15. Kongsricharoern, N.; Polprasert, C. Chromium removal by a bipolar electro-chemical precipitation process. *Water Sci. Technol.* **1996**, *34*, 109–116. [CrossRef]
16. Ramakrishnaiah, C.R.; Prathima, B. Hexavalent chromium removal from industrial wastewater by chemical precipitation method. *Int. J. Eng. Res. Appl.* **2012**, *2*, 599–603.
17. Zhao, Z.; An, H.; Lin, J.; Feng, M.; Murugadoss, V.; Ding, T.; Liu, H.; Shao, Q.; Mai, X.; Wang, N.; et al. Progress on the photocatalytic reduction removal of chromium contamination. *Chem. Rec.* **2019**, *19*, 873–882. [CrossRef]
18. Kongsricharoern, N.; Polprasert, C. Electrochemical precipitation of chromium (Cr^{6+}) from an electroplating wastewater. *Water Sci. Technol.* **1995**, *31*, 109–117. [CrossRef]
19. Mohan, D.; Pittman, C.U., Jr. Activated carbons and low cost adsorbents for remediation of tri- and hexavalent chromium from water. *J. Hazard. Mater.* **2006**, *137*, 762–811. [CrossRef]
20. Pakade, V.E.; Tavengwa, N.T.; Madikizela, L.M. Recent advances in hexavalent chromium removal from aqueous solutions by adsorptive methods. *RSC Adv.* **2019**, *9*, 26142–26164. [CrossRef]
21. Gupta, V.; Agarwal, S.; Saleh, T.A. Chromium removal by combining the magnetic properties of iron oxide with adsorption properties of carbon nanotubes. *Water Res.* **2011**, *45*, 2207–2212. [CrossRef]
22. Peng, H.; Guo, J. Removal of chromium from wastewater by membrane filtration, chemical precipitation, ion exchange, adsorption electrocoagulation, electrochemical reduction, electrodialysis, electrodeionization, photocatalysis and nanotechnology: A review. *Environ. Chem. Lett.* **2020**, *18*, 2055–2068. [CrossRef]
23. Joshi, K.M.; Shrivastava, V.S. Photocatalytic degradation of Chromium (VI) from wastewater using nanomaterials like TiO_2, ZnO, and CdS. *Appl. Nanosci.* **2011**, *1*, 147–155. [CrossRef]
24. Litter, M.I. Last advances on TiO_2-photocatalytic removal of chromium, uranium and arsenic. *Curr. Opin. Green Sustain. Chem.* **2017**, *6*, 150–158. [CrossRef]
25. Gupta, V.K.; Chandra, R.; Tyagi, I.; Verma, M. Removal of hexavalent chromium ions using CuO nanoparticles for water purification applications. *J. Colloid Interface Sci.* **2016**, *478*, 54–62. [CrossRef] [PubMed]
26. Zhao, Y.; Li, L.; Zuo, Y.; He, G.; Chen, Q.; Meng, Q.; Chen, H. Reduced graphene oxide supported ZnO/CdS heterojunction enhances photocatalytic removal efficiency of hexavalent chromium from aqueous solution. *Chemosphere* **2022**, *286*, 131738. [CrossRef]
27. Sukumar, S.; Rudrasenan, A.; Nambiar, D.P. Green-Synthesized Rice-Shaped Copper Oxide Nanoparticles Using *Caesalpinia bonducella* Seed Extract and Their Applications. *ACS Omega* **2020**, *5*, 1040–1051. [CrossRef]
28. Hong, Z.S.; Cao, Y.; Deng, J.F. A convenient alcohothermal approach for low temperature synthesis of CuO nanoparticles. *Mater. Lett.* **2002**, *52*, 34–38. [CrossRef]
29. Li, Z.; Lv, H.; Wang, Z.; Gu, A.; He, X.; Wang, L. In situ growth of $CuCo_2S_4$ nanocrystals on N, S-codoped reduced graphene oxide nanosheets for supercapacitors. *Mater. Res. Express* **2019**, *6*, 085523. [CrossRef]
30. Wang, H.; Xu, J.-Z.; Zhu, J.-J.; Chen, H.-Y. Preparation of CuO nanoparticles by microwave irradiation. *J. Cryst. Growth* **2002**, *244*, 88–94. [CrossRef]
31. Phiwdang, K.; Suphankij, S.; Mekprasart, W.; Pecharapa, W. Synthesis of CuO nanoparticles by precipitation method using different precursors. *Energy Procedia* **2013**, *34*, 740–745. [CrossRef]
32. Saif, S.; Tahir, A.; Asim, T.; Chen, Y. Plant mediated green synthesis of CuO nanoparticles: Comparison of toxicity of engineered and plant mediated CuO nanoparticles towards Daphnia magna. *Nanomaterials* **2016**, *6*, 205. [CrossRef] [PubMed]
33. Bouafia, A.; Laouini, S.E.; Ouahrani, M.R. A review on green synthesis of CuO nanoparticles using plant extract and evaluation of antimicrobial activity. *Asian J. Res. Chem.* **2020**, *13*, 65–70. [CrossRef]
34. Devi, H.S.; Singh, T.D. Synthesis of copper oxide nanoparticles by a novel method and its application in the degradation of methyl orange. *Adv. Electron. Electr. Eng.* **2014**, *4*, 83–88.
35. Dabhane, H.; Ghotekar, S.; Zate, M.; Lin, K.-Y.A.; Rahdar, A.; Ravindran, B.; Bahiram, D.; Ingale, C.; Khairnar, B.; Sali, D.; et al. A novel approach toward the bio-inspired synthesis of CuO nanoparticles for phenol degradation and antimicrobial applications. *Biomass Convers. Biorefinery* **2023**, 1–16. [CrossRef]
36. Chandra, P.; Sinha, S.; Rai, U.N. *Bioremediation of Chromium from Water and Soil by Vascular Aquatic Plants, in Phytoremediation of Soil and Water Contaminants*; American Chemical Society: Washington, DC, USA, 1997; pp. 274–282.
37. Vattikuti, S.P.; Reddy, B.P.; Byon, C.; Shim, J. Carbon/CuO nanosphere-anchored g-C3N4 nanosheets as ternary electrode material for supercapacitors. *J. Solid State Chem.* **2018**, *262*, 106–111. [CrossRef]
38. Weyl, P.; Coetzee, J. The invasion status of *Myriophyllum spicatum* L. in southern Africa. *Manag. Aquat. Invasions* **2014**, *5*, 31–37.

39. Tejaswini, G. A Systematic Investigation on Elaeocarpus Sylvestris Leaf Extract Capped Cuo Nanoparticles as Reducing Agent and Their Antioxidant Activity. *Colloid Polym. Sci.* **2023**, 1–12.

40. Chauhan, M.; Sharma, B.; Kumar, R.; Chaudhary, G.R.; Hassan, A.A.; Kumar, S. Green synthesis of CuO nanomaterials and their proficient use for organic waste removal and antimicrobial application. *Environ. Res.* **2019**, *168*, 85–95. [CrossRef]

41. Hassan, S.E.-D.; Fouda, A.; Radwan, A.A.; Salem, S.S.; Barghoth, M.G.; Awad, M.A.; Abdo, A.M.; El-Gamal, M.S. Endophytic actinomycetes *Streptomyces* spp. mediated biosynthesis of copper oxide nanoparticles as a promising tool for biotechnological applications. *JBIC J. Biol. Inorg. Chem.* **2019**, *24*, 377–393. [CrossRef]

42. Singh, J.; Kumar, V.; Kim, K.H.; Rawat, M. Biogenic synthesis of copper oxide nanoparticles using plant extract and its prodigious potential for photocatalytic degradation of dyes. *Environ. Res.* **2019**, *177*, 108569. [CrossRef]

43. Kasi, S.D.; Ramasamy, J.M.; Nagaraj, D.; Santiyagu, V.; Ponraj, J.S. Biogenic synthesis of copper oxide nanoparticles using leaf extracts of Cissus quadrangularis and Piper betle and its antibacterial effects. *Micro Nano Lett.* **2021**, *16*, 419–424. [CrossRef]

44. Ethiraj, A.S.; Kang, D.J. Synthesis and characterization of CuO nanowires by a simple wet chemical method. *Nanoscale Res. Lett.* **2012**, *7*, 70. [CrossRef] [PubMed]

45. Döring, G.; Sternemann, C.; Kaprolat, A.; Mattila, A.; Hämäläinen, K.; Schülke, W. Shake-up valence excitations in CuO by resonant inelastic X-ray scattering. *Phys. Rev. B* **2004**, *70*, 085115. [CrossRef]

46. Su, D.; Xie, X.; Dou, S.; Wang, G. CuO single crystal with exposed {001} facets-A highly efficient material for gas sensing and Li-ion battery applications. *Sci. Rep.* **2014**, *4*, 5753. [CrossRef] [PubMed]

47. Arunkumar, B.; Jeyakumar, S.J.; Jothibas, M. A sol-gel approach to the synthesis of CuO nanoparticles using Lantana camara leaf extract and their photo catalytic activity. *Optik* **2019**, *183*, 698–705. [CrossRef]

48. Sulaiman, G.M.; Tawfeeq, A.T.; Jaaffer, M.D. Biogenic synthesis of copper oxide nanoparticles using olea europaea leaf extract and evaluation of their toxicity activities: An in vivo and in vitro study. *Biotechnol. Prog.* **2018**, *34*, 218–230. [CrossRef]

49. Waris, A.; Din, M.; Ali, A.; Ali, M.; Afridi, S.; Baset, A.; Khan, A.U. A comprehensive review of green synthesis of copper oxide nanoparticles and their diverse biomedical applications. *Inorg. Chem. Commun.* **2021**, *123*, 108369. [CrossRef]

50. Joshi, N.C.; Prakash, Y.A. Leaves extract-based biogenic synthesis of cupric oxide nanoparticles, characterizations, and antimicrobial activity. *Asian J. Pharm. Clin. Res.* **2019**, *12*, 288–291.

51. Usha, V.; Kalyanaraman, S.; Thangavel, R.; Vettumperumal, R. Effect of catalysts on the synthesis of CuO nanoparticles: Structural and optical properties by sol–gel method. *Superlattices Microstruct.* **2015**, *86*, 203–210. [CrossRef]

52. Zaman, M.B.; Poolla, R.; Singh, P.; Gudipati, T. Biogenic synthesis of CuO nanoparticles using Tamarindus indica L. and a study of their photocatalytic and antibacterial activity. Environmental Nanotechnology. *Monit. Manag.* **2020**, *14*, 100346.

53. Kumar, R.; Kaur, J.; Rawat, M.; Alarfaj, A.A.; Acevedo, R.; Cascione, M.; De Matteis, V.; Singh, J. Biogenic synthesis of CuO nanoparticles for efficient photocatalytic degradation of industrial pollutants. *Hum. Ecol. Risk Assess. Int. J.* **2023**, *29*, 927–937. [CrossRef]

54. Singh, P.; Singh, K.R.; Singh, J.; Singh, R.P. Biogenic synthesis of copper oxide nanoparticles: Characterization and biosensing application. *ECS Trans.* **2022**, *107*, 20127. [CrossRef]

55. Felix, S.; Chakkravarthy, R.B.; Grace, A.N. Microwave assisted synthesis of copper oxide and its application in electrochemical sensing. In *IOP Conference Series: Materials Science and Engineering*; IOP Publishing: Kerala, India, 2015.

56. Vaseem, M.; Umar, A.; Hahn, Y.; Kim, D.; Lee, K.; Jang, J.; Lee, J. Flower-shaped CuO nanostructures: Structural, photocatalytic and XANES studies. *Catal. Commun.* **2008**, *10*, 11–16. [CrossRef]

57. Liu, Q.; Liang, Y.; Liu, H.; Hong, J.; Xu, Z. Solution phase synthesis of CuO nanorods. *Mater. Chem. Phys.* **2006**, *98*, 519–522. [CrossRef]

58. Sagadevan, S.; Pal, K.; Chowdhury, Z.Z. Fabrication of CuO nanoparticles for structural, optical and dielectric analysis using chemical precipitation method. *J. Mater. Sci. Mater. Electron.* **2017**, *28*, 12591–12597. [CrossRef]

59. Boltaev, G.S.; Ganeev, R.A.; Krishnendu, P.S.; Zhang, K.; Guo, C. Nonlinear optical characterization of copper oxide nanoellipsoids. *Sci. Rep.* **2019**, *9*, 11414. [CrossRef] [PubMed]

60. Anandan, S.; Yang, S. Emergent methods to synthesize and characterize semiconductor CuO nanoparticles with various morphologies—An overview. *J. Exp. Nanosci.* **2007**, *2*, 23–56. [CrossRef]

61. Poornaprakash, B.; Chalapathi, U.; Suh, Y.; Vattikuti, S.P.; Reddy, M.S.P.; Park, S.-H. Terbium-doped ZnS quantum dots: Structural, morphological, optical, photoluminescence, and photocatalytic properties. *Ceram. Int.* **2018**, *44*, 11724–11729. [CrossRef]

62. Reddy, K.R. Green synthesis, morphological and optical studies of CuO nanoparticles. *J. Mol. Struct.* **2017**, *1150*, 553–557. [CrossRef]

63. Anthony, E.T.; Oladoja, N.A. Process enhancing strategies for the reduction of Cr (VI) to Cr (III) via photocatalytic pathway. *Environ. Sci. Pollut. Res.* **2022**, *29*, 8026–8053. [CrossRef]

64. Shao, D.; Wang, X.; Fan, Q. Photocatalytic reduction of Cr (VI) to Cr (III) in solution containing ZnO or ZSM-5 zeolite using oxalate as model organic compound in environment. *Microporous Mesoporous Mater.* **2009**, *117*, 243–248. [CrossRef]

65. Liu, W.; Ni, J.; Yin, X. Synergy of photocatalysis and adsorption for simultaneous removal of Cr (VI) and Cr (III) with TiO_2 and titanate nanotubes. *Water Res.* **2014**, *53*, 12–25. [CrossRef] [PubMed]

66. Idris, A.; Majidnia, Z.; Kamarudin, K.S.B.N. Photocatalyst treatment for lead (II) using titanium oxide nanoparticles embedded in PVA-alginate beads. *Water Treat.* **2016**, *57*, 5035–5044. [CrossRef]

67. Murruni, L.; Leyva, G.; Litter, M.I. Photocatalytic removal of Pb (II) over TiO$_2$ and Pt–TiO$_2$ powders. *Catal. Today* **2007**, *129*, 127–135. [CrossRef]

68. Litter, M.I. Mechanisms of removal of heavy metals and arsenic from water by TiO$_2$-heterogeneous photocatalysis. *Pure Appl. Chem.* **2015**, *87*, 557–567. [CrossRef]

69. Umadevi, M.; Christy, A.J. Synthesis, characterization and photocatalytic activity of CuO nanoflowers. *Spectrochim. Acta Part A Mol. Biomol. Spectrosc.* **2013**, *109*, 133–137. [CrossRef]

70. Sibhatu, A.K.; Weldegebrieal, G.K.; Sagadevan, S.; Tran, N.N.; Hessel, V. Photocatalytic activity of CuO nanoparticles for organic and inorganic pollutants removal in wastewater remediation. *Chemosphere* **2022**, *200*, 134623. [CrossRef]

71. Saravanakumar, K.; Karthik, R.; Chen, S.M.; Kumar, J.V.; Prakash, K.; Muthuraj, V. Construction of novel Pd/CeO$_2$/g-C$_3$N$_4$ nanocomposites as efficient visible-light photocatalysts for hexavalent chromium detoxification. *J. Colloid Interface Sci.* **2017**, *504*, 514–526. [CrossRef]

72. Lin, Z.; Zheng, Y.; Deng, F.; Luo, X.; Zou, J.; Shao, P.; Zhang, S.; Tang, H. Target-directed design of dual-functional Z-scheme AgIn5S8/SnS2 heterojunction for Pb (II) capture and photocatalytic reduction of Cr (VI): Performance and mechanism insight. *Sep. Purif. Technol.* **2021**, *277*, 119430. [CrossRef]

73. Samuel, M.S.; Ravikumar, M.; John, J.A.; Selvarajan, E.; Patel, H.; Chander, P.S.; Soundarya, J.; Vuppala, S.; Balaji, R.; Chandrasekar, N. A Review on Green Synthesis of Nanoparticles and Their Diverse Biomedical and Environmental Applications. *Catalysts* **2022**, *12*, 459. [CrossRef]

74. Dulta, K.; Ağçeli, G.K.; Chauhan, P.; Jasrotia, R.; Ighalo, J.O. Multifunctional CuO nanoparticles with enhanced photocatalytic dye degradation and antibacterial activity. *Sustain. Environ. Res.* **2022**, *32*, 2. [CrossRef]

75. Hossain, S.S.; Tarek, M.; Munusamy, T.D.; Karim, K.M.; Roopan, S.M.; Sarkar, S.M.; Cheng, C.K.; Khan, M.M. Facile synthesis of CuO/CdS heterostructure photocatalyst for the effective degradation of dye under visible light. *Environ. Res.* **2020**, *188*, 109803. [CrossRef] [PubMed]

76. Ramesh, M. CuO as efficient photo catalyst for photocatalytic decoloration of wastewater containing Azo dyes. *Water Pract. Technol.* **2021**, *16*, 1078–1090. [CrossRef]

77. Ravele, M.P.; Oyewo, O.A.; Ramaila, S.; Mavuru, L.; Onwudiwe, D.C. Photocatalytic Degradation of Tetracycline in Aqueous Solution Using Copper Sulfide Nanoparticles. *Catalysts* **2021**, *11*, 1238. [CrossRef]

78. Xu, L.; Su, J.; Zheng, G.; Zhang, L. Enhanced photocatalytic performance of porous ZnO thin films by CuO nanoparticles surface modification. *Mater. Sci. Eng. B* **2019**, *248*, 114405. [CrossRef]

79. Kumar, P.S.; Selvakumar, M.; Babu, S.G.; Jaganathan, S.K.; Karuthapandian, S.; Chattopadhyay, S. Novel CuO/chitosan nanocomposite thin film: Facile hand-picking recoverable, efficient and reusable heterogeneous photocatalyst. *RSC Adv.* **2015**, *5*, 57493–57501. [CrossRef]

80. Mohagheghian, A.; Besharati-Givi, N.; Godini, K.; Dewil, R.; Shirzad-Siboni, M. Photocatalytic reduction of Cr(VI) from aqueous solution by visible light/CuO-Kaolin: Optimization and modeling of key parameters using central composite design (CCD). *Sep. Sci. Technol.* **2021**, *56*, 1253–1271. [CrossRef]

81. Yan, X.; Song, M.; Zhou, M.; Ding, C.; Wang, Z.; Wang, Y.; Yang, W.; Yang, Z.; Liao, Q.; Shi, Y. Response of Cupriavidus basilensis B-8 to CuO nanoparticles enhances Cr(VI) reduction. *Sci. Total Environ.* **2019**, *688*, 46–55. [CrossRef]

82. Choudhury, P.; Mondal, P.; Majumdar, S.; Saha, S.; Sahoo, G.C. Preparation of ceramic ultrafiltration membrane using green synthesized CuO nanoparticles for chromium (VI) removal and optimization by response surface methodology. *J. Clean. Prod.* **2018**, *203*, 511–520. [CrossRef]

83. Koysuren, O.; Koysuren, H.N. Application of CuO and its composite with polyaniline on the photocatalytic degradation of methylene blue and the Cr(VI) photoreduction under visible light. *J. Sol-Gel Sci. Technol.* **2023**, *106*, 131–148. [CrossRef]